

Topological Insulators in Twisted Transition Metal Dichalcogenide Homobilayers


Fengcheng Wu,^{1,2} Timothy Lovorn,³ Emanuel Tutuc,⁴ Ivar Martin,¹ and A. H. MacDonald³

¹Materials Science Division, Argonne National Laboratory, Argonne, Illinois 60439, USA

²Condensed Matter Theory Center and Joint Quantum Institute, Department of Physics, University of Maryland, College Park, Maryland 20742, USA

³Department of Physics, University of Texas at Austin, Austin, Texas 78712, USA

⁴Department of Electrical and Computer Engineering, Microelectronics Research Center, The University of Texas at Austin, Austin, Texas 78758, USA

 (Received 9 July 2018; published 28 February 2019)

We show that moiré bands of twisted homobilayers can be topologically nontrivial, and illustrate the tendency by studying valence band states in $\pm K$ valleys of twisted bilayer transition metal dichalcogenides, in particular, bilayer MoTe_2 . Because of the large spin-orbit splitting at the monolayer valence band maxima, the low energy valence states of the twisted bilayer MoTe_2 at the $+K$ ($-K$) valley can be described using a two-band model with a layer-pseudospin magnetic field $\Delta(\mathbf{r})$ that has the moiré period. We show that $\Delta(\mathbf{r})$ has a topologically nontrivial skyrmion lattice texture in real space, and that the topmost moiré valence bands provide a realization of the Kane-Mele quantum spin-Hall model, i.e., the two-dimensional time-reversal-invariant topological insulator. Because the bands narrow at small twist angles, a rich set of broken symmetry insulating states can occur at integer numbers of electrons per moiré cell.

DOI: [10.1103/PhysRevLett.122.086402](https://doi.org/10.1103/PhysRevLett.122.086402)

Introduction.—Moiré superlattices form in van der Waals bilayers with small differences between the lattice constants or orientations of the individual layers, and often dramatically alter electronic properties [1–6]. In the presence of long-period moiré patterns, electronic states can be described by continuum model Hamiltonians with the moiré periodicity and spinors whose dimension is equal to the total number of bands, summed over layers, in the energy range of interest. Application of Bloch’s theorem then gives rise to moiré bands [7]. Because the moiré pattern often generates spatial confinement, moiré bands can be narrow, enhancing the importance of electronic correlations. The flat bands of magic-angle twisted bilayer graphene, in which correlated insulating and superconducting states have been discovered [8,9], provide a prominent example. The study of moiré flat bands has recently become an active area of experimental and theoretical research centered on efforts to identify promising bilayer structures, and on topological characterization and many-body interaction physics [10–15].

When the two layers are formed from the same material (homobilayers), both must be treated on equal footing. The $\pm K$ -valley valence bands of semiconductor group-VI transition metal dichalcogenide (TMD) monolayers provide a prototypical model system because strong spin-orbit coupling and broken inversion symmetry lifts spin degeneracy [16], and the corresponding homobilayer can be described by a two-band model with layer pseudospins at each valley. The moiré pattern’s periodic modulation can then be accounted for by a scalar potential and a

pseudomagnetic field $\Delta(\mathbf{r})$ whose components are the coefficients of the layer Pauli matrix expansion of the two-band Hamiltonian; i.e., Δ_x and Δ_y are the real and imaginary parts of the interlayer tunneling amplitude and Δ_z is the potential difference between layers. The field $\Delta(\mathbf{r})$ inherits the moiré pattern periodicity and plays a key role in the discussion below.

In this Letter, we focus on the MoTe_2 bilayer with AA stacking [Fig. 1], for which valence band maxima are located in $\pm K$ valleys according to our first-principles calculations as shown in the Supplemental Material (SM) [17]. For this system, we find that $\Delta(\mathbf{r})$ has a skyrmion lattice texture in real space, and that the moiré bands carry valley-contrasting Chern numbers. The topological moiré bands can provide a realization of the Kane-Mele model, where the effective gauge potential is generated by the

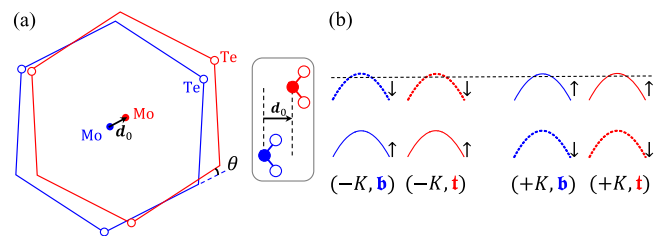


FIG. 1. (a) Top view of AA stacked MoTe_2 homobilayer with a small twist angle θ and an in-plane displacement d_0 . The inset is a schematic side view. (b) $\pm K$ valence bands in the AA stacking case when interlayer coupling is neglected.

momentum shift between the two twisted layers. When the bilayer is polarized by a vertical displacement potential, the band Chern numbers are driven to zero before $\Delta(\mathbf{r})$ becomes topologically trivial in real space. In partially filled topological flat bands, interactions can, e.g., break time-reversal symmetry to form quantum anomalous Hall states.

Aligned bilayers.—To derive a moiré continuum Hamiltonian, we start by analyzing the electronic structure of an aligned bilayer [21]. Because the $\pm K$ valleys are related by time-reversal symmetry \hat{T} , we can focus on the $+K$ valley. In an AA stacked TMD homobilayer [Fig. 1], the valence states at the $+K$ valley valence band maximum are mainly of $d_{x^2-y^2} + id_{xy}$ orbital character, have spin up (\uparrow) along \hat{z} axis [16], and are separated from spin-down (\downarrow) states by strong spin-orbit splitting. Retaining only the spin up valence-band states at the $+K$ valley yields the two-band $k \cdot p$ Hamiltonian [17],

$$\mathcal{H}_{\uparrow}(\theta=0, \mathbf{d}_0) = \begin{pmatrix} -\frac{\hbar^2 k^2}{2m^*} + \Delta_{\mathfrak{b}}(\mathbf{d}_0) & \Delta_T(\mathbf{d}_0) \\ \Delta_T^\dagger(\mathbf{d}_0) & -\frac{\hbar^2 k^2}{2m^*} + \Delta_{\mathfrak{t}}(\mathbf{d}_0) \end{pmatrix}, \quad (1)$$

with parameters that depend on the displacement \mathbf{d}_0 between the aligned layers. In Eq. (1), \mathfrak{b} and \mathfrak{t} refer to bottom (\mathfrak{b}) and top (\mathfrak{t}) layers, \mathbf{k} is momentum measured from the $+K$ point, m^* is the valence band effective mass that is approximately independent of \mathbf{d}_0 [17], $\Delta_{\mathfrak{b},\mathfrak{t}}$ are layer-dependent energies, and Δ_T is an interlayer tunneling amplitude. The dependence of Δ_α ($\alpha = \mathfrak{b}, \mathfrak{t}, T$) on \mathbf{d}_0 is constrained by the symmetry properties of the bilayer. The two-dimensional lattice periodicity of the aligned bilayers implies that the Δ_α are periodic functions of \mathbf{d}_0 . A $z \leftrightarrow -z$ mirror operation interchanges \mathfrak{b} and \mathfrak{t} and maps displacement \mathbf{d}_0 to $-\mathbf{d}_0$, implying that $\Delta_{\mathfrak{t}}(\mathbf{d}_0) = \Delta_{\mathfrak{b}}(-\mathbf{d}_0)$. Threefold rotation around the \hat{z} axis requires that $\Delta_{\mathfrak{b}}$ and $\Delta_{\mathfrak{t}}$ be invariant when \mathbf{d}_0 is rotated by $2\pi/3$. These symmetry constraints lead to the following two-parameter lowest-harmonic parametrization:

$$\Delta_\ell(\mathbf{d}_0) = 2V \sum_{j=1,3,5} \cos(\mathbf{G}_j \cdot \mathbf{d}_0 + \ell\psi), \quad (2)$$

where $\ell = 1$ for the \mathfrak{b} layer and $\ell = -1$ for the \mathfrak{t} layer, \mathbf{G}_j is the reciprocal lattice vector obtained by counterclockwise rotation of $\mathbf{G}_1 = (4\pi)/(\sqrt{3}a_0)\hat{y}$ by angle $(j-1)\pi/3$, a_0 is the monolayer TMD lattice constant, and V and ψ , respectively, characterize the amplitude and shape of the potentials. Note that we have chosen the spatial averages of $\Delta_{\mathfrak{b},\mathfrak{t}}$, which must be identical, as the zero of energy.

The \mathbf{d}_0 dependence of Δ_T is most conveniently understood by assuming a two-center approximation [7] for tunneling between the metal $d_{x^2-y^2} + id_{xy}$ orbitals, and using a lowest-harmonic approximation. This leads to

$$\Delta_T(\mathbf{d}_0) = w(1 + e^{-iG_2 \cdot \mathbf{d}_0} + e^{-iG_3 \cdot \mathbf{d}_0}), \quad (3)$$

where w is a tunneling strength parameter. It is informative to highlight three high-symmetry displacement values: $\mathbf{d}_{0,n} = n(\mathbf{a}_1 + \mathbf{a}_2)/3$ for $n = 0, \pm 1$, where $\mathbf{a}_{1,2}$ are the primitive translation vectors of the aligned bilayer: $\mathbf{a}_1 = a_0(1, 0)$ and $\mathbf{a}_2 = a_0(1/2, \sqrt{3}/2)$. For $n = 0$ the metal atoms of the two layers are aligned, $\Delta_{\mathfrak{t}} = \Delta_{\mathfrak{b}} = 6V \cos(\psi)$ and $\Delta_T = 3w$; the valence band maximum states are then symmetric and antisymmetric combinations of the isolated layer states. For $n = \pm 1$ the metal atoms in one layer are aligned with the chalcogen atoms in the other layer, and Δ_T vanishes as a result of the threefold rotational symmetry \hat{C}_{3z} . We determine the model parameters by fitting the eigenvalues of $\mathcal{H}_{\uparrow}(\mathbf{k} = 0)$ at the three displacements to corresponding values from fully relativistic band structure calculations using QUANTUM ESPRESSO [22]. We find that $(V, \psi, w) \approx (8 \text{ meV}, -89.6^\circ, -8.5 \text{ meV})$ for MoTe₂.

Moiré Hamiltonian.—We construct the twisted bilayer Hamiltonian by starting from an aligned bilayer with $\mathbf{d}_0 = 0$ and then rotating the bottom and top layers by angles $-\theta/2$ and $+\theta/2$ around a metal site. (Any initial displacement just shifts the moiré pattern globally [7,23].) We take the origin of coordinates to be on this rotation axis and midway between layers. With respect to this origin, the bilayer has D_3 point group symmetry generated by the threefold rotation \hat{C}_{3z} around \hat{z} axis and a twofold rotation \hat{C}_{2y} around \hat{y} axis that swaps the two layers. In a long-period moiré pattern, the local displacement between the two layers, approximated by $\theta\hat{z} \times \mathbf{r}$, varies smoothly with the spatial position \mathbf{r} [21,24]. The moiré Hamiltonian is

$$\mathcal{H}_{\uparrow} = \begin{pmatrix} -\frac{\hbar^2(k-\kappa_+)^2}{2m^*} + \Delta_{\mathfrak{b}}(\mathbf{r}) & \Delta_T(\mathbf{r}) \\ \Delta_T^\dagger(\mathbf{r}) & -\frac{\hbar^2(k-\kappa_-)^2}{2m^*} + \Delta_{\mathfrak{t}}(\mathbf{r}) \end{pmatrix}, \quad (4)$$

where $\Delta_\alpha(\mathbf{r})$ is obtained by replacing \mathbf{d}_0 in Eqs. (2)–(3) with $\theta\hat{z} \times \mathbf{r}$ to account for the spatial variation of the local inter-layer coordination. The moiré Hamiltonian is periodic with the moiré period $a_M = a_0/\theta$. Because of the twist, the $+K$ points associated with the bottom and top layers are rotated to different momenta, accounted for by the κ_{\pm} shifts in Eq. (4). We choose a moiré Brillouin zone (MBZ) in which the κ_{\pm} points are located at the MBZ corners, as illustrated in Fig. 2(a).

To reveal the spatial structure of the Δ_α field, we define the layer pseudospin magnetic field:

$$\Delta(\mathbf{r}) = (\Delta_x, \Delta_y, \Delta_z) \equiv \left(\text{Re}\Delta_T^\dagger, \text{Im}\Delta_T^\dagger, \frac{\Delta_{\mathfrak{b}} - \Delta_{\mathfrak{t}}}{2} \right). \quad (5)$$

As illustrated in Fig. 2(b), $\Delta_z(\mathbf{r})$ vanishes along the links that connect nearest-neighbor \mathcal{R}_M^M sites and has minimum and maximum values at \mathcal{R}_M^X and \mathcal{R}_X^M . The in-plane pseudospin field, which accounts for interlayer tunneling,

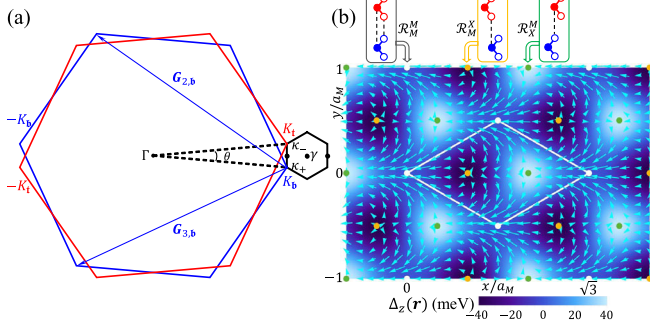


FIG. 2. (a) Brillouin zones of the bottom (blue) and top (red) layers in a twisted bilayer, and the moiré Brillouin zone (black). (b) The $+K$ -valley layer pseudospin skyrmion lattice in the moiré pattern. The color map illustrates the variation of Δ_z , and the arrows indicate $\Delta_{x,y}$. The white lines outline a single moiré unit cell. The dots indicate the high symmetry positions \mathcal{R}_M^M , \mathcal{R}_X^M , and \mathcal{R}_M^X , where the local interlayer displacements are respectively $d_{0,0}$, $d_{0,1}$, and $d_{0,-1}$.

has vortex and antivortex structures centered on \mathcal{R}_M^X and \mathcal{R}_X^M . Here \mathcal{R}_α^β denotes high-symmetry sites at which α atoms of the bottom layer are locally aligned with β atoms of the top layer. It follows that $\Delta(\mathbf{r})$ forms a skyrmion lattice, i.e., that the direction of the $\Delta(\mathbf{r})$ covers the unit sphere once in each moiré unit cell (MUC). We have explicitly confirmed this property by numerically evaluating the winding number [25]:

$$N_w \equiv \frac{1}{4\pi} \int_{\text{MUC}} d\mathbf{r} \frac{\Delta \cdot (\partial_x \Delta \times \partial_y \Delta)}{|\Delta|^3} = -1. \quad (6)$$

Skyrmion lattice pseudospin textures in position space indicate [26] the possibility of topological electronic bands in momentum space, although we will find that the connection is not one to one.

Topological bands.—The moiré band structure is illustrated in Fig. 3(a) for a representative angle $\theta = 1.2^\circ$. The $\hat{C}_{2y}\hat{T}$ symmetry of the Hamiltonian maps $\kappa_+ \rightarrow \kappa_-$ and therefore enforces degeneracy between these points. For the two topmost moiré bands of the $+K$ valley, wave functions in the \mathbf{b} (\mathbf{t}) layer are concentrated near the \mathcal{R}_X^M (\mathcal{R}_M^X) sites, which are Δ_b (Δ_t) maxima. Because of the layer-dependent momentum shifts κ_\pm in the kinetic energies, the moiré band wave functions vary rapidly over the MBZ. In particular, the wave function of the topmost moiré band at κ_+ and κ_- are respectively localized in layers \mathbf{b} and \mathbf{t} . By integrating the Berry curvature \mathcal{F} over the MBZ [27], we confirm that the Chern numbers \mathcal{C} of the two topmost $+K$ valley moiré bands in Fig. 3 are nontrivial ($\mathcal{C} = \pm 1$) at $\theta = 1.2^\circ$. The corresponding bands at the $-K$ valley must have the opposite Chern numbers due to the \hat{T} symmetry. Spin-valley locking implies that when the chemical potential is in the gap between the two topmost bands, the twisted

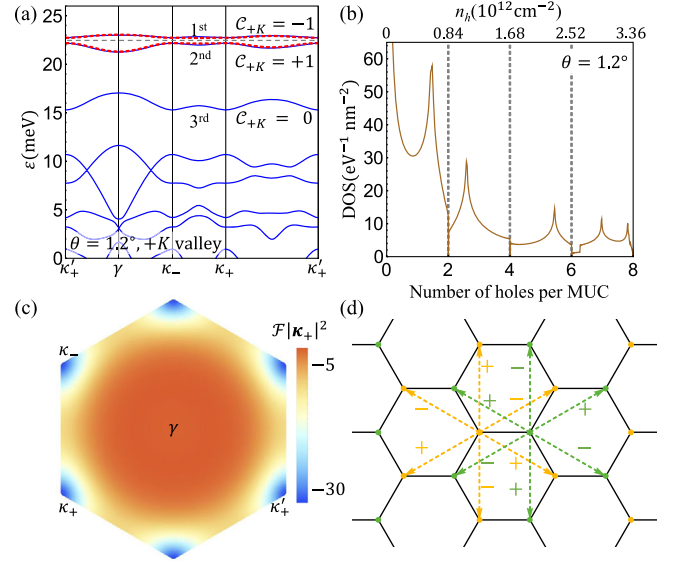


FIG. 3. (a) Moiré band structure at twist angle 1.2° . The system is a topological insulator when the chemical potential (black dashed line) is in the gap between the first and second bands. The red dashed lines are a tight-binding-model fit based on the effective Hamiltonian Eq. (7) with $t_0 \approx 0.29$ meV and $t_1 \approx 0.06$ meV. (b) Total density of states (DOS) as a function of the number of holes per moiré unit cell (bottom) and per area (top). (c) Berry curvature \mathcal{F} for the first band in (a). Here the typical magnitude of \mathcal{F} is 3 orders of magnitude larger than that in the monolayer [16,17]. (d) Illustration of the tight-binding model (7). The yellow and green dots represent \mathcal{R}_M^X and \mathcal{R}_X^M sites, and together form a honeycomb lattice. The signs \pm refer to the bond and spin dependent hopping phase factors $\exp(\pm i2\pi s/3)$.

homobilayer is not only a valley Hall insulator but also a quantum spin Hall insulator, i.e., a topological insulator [28,29].

To gain deeper insight into the topological bands, we construct a tight-binding model. The real space distribution of the wave functions suggests a two-orbital model for the first two moiré bands:

$$H_{\text{TB}} = \sum_{\ell,s} \sum_{\mathbf{R}\mathbf{R}'} t_0 c_{\mathbf{R}\ell s}^\dagger c_{\mathbf{R}'(-\ell)s} + \sum_{\ell,s} \sum_{\mathbf{R}} \sum_{\mathbf{a}_M} t_1 e^{i\mathbf{s}\kappa_\ell \cdot \mathbf{a}_M} c_{(\mathbf{R}+\mathbf{a}_M)\ell s}^\dagger c_{\mathbf{R}\ell s}, \quad (7)$$

where $s = \pm$ denotes spin (equivalent to valley $\pm K$), and $\ell = \pm$ labels orbitals localized in the bottom (+1) and top (-1) layers and centered around the \mathcal{R}_X^M and \mathcal{R}_M^X sites. The two orbitals form a honeycomb lattice in Fig. 3(d). In Eq. (7), the spin up and down sectors are decoupled due to the spin-valley $U(1)$ symmetry of the low-energy theory, and are related by \hat{T} symmetry. The first line of Eq. (7) captures interlayer hopping between nearest neighbors on the honeycomb lattice. Its form is constrained by the requirements that the energy spectra have threefold

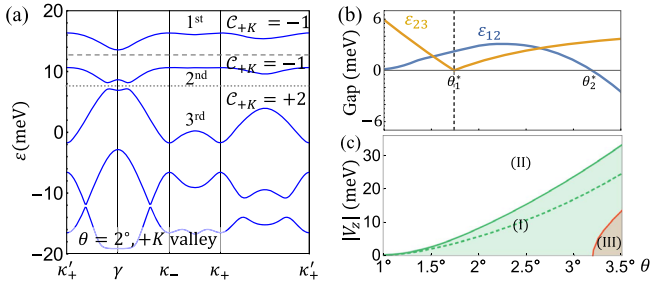


FIG. 4. (a) Moiré bands at twist angle 2° . (b) Energy gaps between adjacent moiré bands as a function of θ . The gap ε_{ij} is the difference between the minimum energy of band i and the maximum energy of band j . (c) Phase diagram as a function of angle θ and layer bias potential V_z . When the chemical potential is in the gap between the first and the second band, the system is a topological insulator in region (I) and a trivial insulator in region (II). In region (III), the two bands overlap in energy. The solid and dashed green lines show the critical bias potentials obtained using the full moiré Hamiltonian and the effective tight-binding model, respectively. (b) and (c) have the same horizontal axis.

rotational symmetry and be identical at κ_+ and κ_- points. The second line of Eq. (7) captures intralayer hopping between next nearest neighbors on the honeycomb lattice; the bond and spin-dependent phase factors $\exp(i s \mathbf{k}_\ell \cdot \mathbf{a}_M)$, which take values of $\exp(\pm i 2\pi/3)$, are analogous to the Peierls substitution and account for the momentum shift \mathbf{k}_ℓ in Eq. (4). The Hamiltonian Eq. (7) is equivalent to the Kane-Mele model [28,29], and to two time-reversed-partner copies of the Haldane model [30]. It correctly captures both the topological character and the energy dispersion of the first two bands in Fig. 3(a).

At a critical angle $\theta_1^* \approx 1.74^\circ$ the gap between the second and the third bands closes at the γ point, as illustrated in Fig. 4. When θ crosses θ_1^* from below, the Chern number of the first band in the $+K$ valley remains as -1 , while the Chern numbers for the second and third bands change from $(+1, 0)$ to $(-1, +2)$. Although, the two-orbital model Eq. (7) is not fully applicable for $\theta > \theta_1^*$ it still captures the main character of the first two bands in regions of momentum space away from the γ point. The system remains as a topological insulator when the chemical potential is in the gap between the first and the second bands until θ reaches $\theta_2^* \approx 3.1^\circ$, beyond which there is no global gap between the first two bands. In the SM [17], we have verified the robustness of our predicted topological bands against perturbation from remote bands.

Field induced topological transition.—Because the two sublattices in Eq. (7) are associated with different layers, a vertical electric field generates a staggered sublattice potential, which can induce a topological phase transition [28–30]. To study this transition, we add a layer dependent potential $\ell V_z/2$ to the moiré Hamiltonian Eq. (4) so that $\Delta_z \rightarrow (\Delta_b - \Delta_t + V_z)/2$. (We neglect the small spatial modulation of V_z due to variation in the vertical distance

between layers in the moiré pattern [31].) The magnitude of V_z has a critical value $|V_z|_c$, at which the gap between the first and the second moiré bands closes at the κ_\pm points. When $|V_z| > |V_z|_c$, wave functions in the first moiré band are primarily localized in one single layer and the band becomes topologically trivial. The tight-binding model Eq. (7) predicts that $|V_z|_c$ is equal to splitting between the first and the second bands at κ_\pm when $V_z = 0$, because the interlayer hopping term in Eq. (7) vanishes at these momenta. In Fig. 4(c) we compare values of $|V_z|_c$ calculated from the tight-binding and the full moiré band Hamiltonian, showing that they match well, particularly for small twist angles (long moiré period). We note that there is no one-to-one correspondence between the Chern numbers \mathcal{C} of the electronic bands and the winding number N_w of the pseudospin field, which remains nontrivial until V_z equals $|\Delta_b - \Delta_t|$ evaluated at the \mathcal{R}_M^X or \mathcal{R}_X^M sites.

Interaction effects.—When the moiré bands are nearly flat, the density of states is strongly enhanced [Fig. 3(b)] and many-body interaction effects are magnified. Here we focus on interaction effects within the first two moiré bands at zero V_z and small θ . The on-site Coulomb repulsion U_0 scales as $e^2/(\epsilon a_w)$, where ϵ is an effective dielectric constant that depends on the three-dimensional dielectric environment, and a_w is the spatial extent of the Wannier orbitals centered at \mathcal{R}_M^X or \mathcal{R}_X^M sites. For θ around 1° , we find that U_0 can be more than one order of magnitude larger than the hopping parameters $t_{0,1}$ [17]. In the strong correlation limit, we anticipate that the interplay between layer and spin or valley degrees of freedom will lead to unusual distinct insulating states at integer numbers of holes per MUC. For one hole per MUC, where the first moiré band is half filled, one candidate insulating state is ferromagnetic. Because the single-particle Hamiltonian has only $U(1)$ symmetry, perpendicular spin polarization is energetically preferred. The Ising spin anisotropy implies finite temperature phase transitions. When the first moiré band is completely spin polarized, the system is a quantum anomalous Hall insulator. Similar physics could occur for three holes per MUC, where the second moiré band is half filled. For two holes per MUC (equivalently one hole per sublattice site of the honeycomb lattice in Kane-Mele model), there is a competition between the quantum spin Hall insulator and the antiferromagnetic insulator [32], which occur for weak and strong interactions, respectively. For some fractional numbers of holes per MUC, the flat bands may host fractional topological insulators [33].

Discussion.—It has been proposed that the Hubbard model can be simulated in TMD *heterobilayers* [10]. In twisted TMD *homobilayers*, the two layers can be effectively decoupled by using a finite layer bias potential to drive the system into region (II) of the phase diagram in Fig. 4(c). Thus, a conventional one-orbital Hubbard model can also be studied in twisted *homobilayers*, with a greater scope for *in situ* manipulation of model parameters.

Compared to heterobilayers, twisted TMD homobilayers may be experimentally realized with a more precise control of the twist angle by using the “tear-and-stack” technique [4,8,9]. Moiré bands with valley-contrasting Chern numbers have been proposed in some graphene-based moiré systems [14,15,34]. In this case, however, quantum spin Hall states that might be induced by interactions cannot survive to accessible temperatures because electrons in graphene have accurate $SU(2)$ spin symmetry which enhances fluctuation effects. In Ref. [35], quantum spin Hall nanodots and nanostripes have been proposed for TMD-based moiré systems in which the large gap between valence and conduction bands needs to be inverted by a strong vertical electric field. In contrast, our model Hamiltonian relies only on valence band states. Our proposal for topological states is based on valley contrast physics and on pseudospin texture in the moiré pattern; the advantage is that it does not require massless chiral fermions in the parent monolayer or aligned bilayer, which may lead to application in a larger class of two-dimensional materials.

F. W. and I. M. are supported by the Department of Energy, Office of Science, Materials Science and Engineering Division. F. W. is also supported by Laboratory for Physical Sciences. Work at Austin is supported by Army Research Office (ARO) Grant No. W911NF-17-1-0312 (MURI) and by the Welch foundation under Grant No. TBF1473. We acknowledge HPC resources provided by the Texas Advanced Computing Center (TACC) at The University of Texas at Austin.

-
- [1] B. Hunt, J. D. Sanchez-Yamagishi, A. F. Young, M. Yankowitz, B. J. LeRoy, K. Watanabe, T. Taniguchi, P. Moon, M. Koshino, P. Jarillo-Herrero, and R. C. Ashoori, *Science* **340**, 1427 (2013).
- [2] C. R. Dean, L. Wang, P. Maher, C. Forsythe, F. Ghahari, Y. Gao, J. Katoch, M. Ishigami, P. Moon, M. Koshino, T. Taniguchi, K. Watanabe, K. L. Shepard, J. Hone, and P. Kim, *Nature (London)* **497**, 598 (2013).
- [3] L. Wang, Y. Gao, B. Wen, Z. Han, T. Taniguchi, K. Watanabe, M. Koshino, J. Hone, and C. R. Dean, *Science* **350**, 1231 (2015).
- [4] K. Kim, A. DaSilva, S. Huang, B. Fallahzad, S. Larentis, T. Taniguchi, K. Watanabe, B. J. LeRoy, A. H. MacDonald, and E. Tutuc, *Proc. Natl. Acad. Sci. U.S.A.* **114**, 3364 (2017).
- [5] E. M. Spanton, A. A. Zibrov, H. Zhou, T. Taniguchi, K. Watanabe, M. P. Zaletel, and A. F. Young, *Science* **360**, 62 (2018).
- [6] G. Chen, L. Jiang, S. Wu, B. Lv, H. Li, K. Watanabe, T. Taniguchi, Z. Shi, Y. Zhang, and F. Wang, *arXiv:1803.01985*.
- [7] R. Bistritzer and A. H. MacDonald, *Proc. Natl. Acad. Sci. U.S.A.* **108**, 12233 (2011).
- [8] Y. Cao, V. Fatemi, A. Demir, S. Fang, S. L. Tomarken, J. Y. Luo, J. D. Sanchez-Yamagishi, K. Watanabe, T. Taniguchi, E. Kaxiras, R. C. Ashoori, and P. Jarillo-Herrero, *Nature (London)* **556**, 80 (2018).
- [9] Y. Cao, V. Fatemi, S. Fang, K. Watanabe, T. Taniguchi, E. Kaxiras, and P. Jarillo-Herrero, *Nature (London)* **556**, 43 (2018).
- [10] F. Wu, T. Lovorn, E. Tutuc, and A. H. MacDonald, *Phys. Rev. Lett.* **121**, 026402 (2018).
- [11] H. C. Po, L. Zou, A. Vishwanath, and T. Senthil, *Phys. Rev. X* **8**, 031089 (2018).
- [12] F. Wu, A. H. MacDonald, and I. Martin, *Phys. Rev. Lett.* **121**, 257001 (2018).
- [13] M. H. Naik and M. Jain, *Phys. Rev. Lett.* **121**, 266401 (2018).
- [14] B. L. Chittari, G. Chen, Y. Zhang, F. Wang, and J. Jung, *Phys. Rev. Lett.* **122**, 016401 (2019).
- [15] Y.-H. Zhang, D. Mao, Y. Cao, P. Jarillo-Herrero, and T. Senthil, *arXiv:1805.08232*.
- [16] D. Xiao, G.-B. Liu, W. Feng, X. Xu, and W. Yao, *Phys. Rev. Lett.* **108**, 196802 (2012).
- [17] See Supplemental Material at <http://link.aps.org/supplemental/10.1103/PhysRevLett.122.086402> for *ab initio* band structure, perturbations from remote bands, additional discussion of interaction effects, and simulation of two-orbital Hubbard model using the AB stacking configuration, which includes Refs. [18–20].
- [18] G.-B. Liu, W.-Y. Shan, Y. Yao, W. Yao, and D. Xiao, *Phys. Rev. B* **88**, 085433 (2013).
- [19] M. K. Agarwal and M. J. Capers, *J. Appl. Crystallogr.* **5**, 63 (1972).
- [20] Y. Wang, Z. Wang, W. Yao, G.-B. Liu, and H. Yu, *Phys. Rev. B* **95**, 115429 (2017).
- [21] J. Jung, A. Raoux, Z. Qiao, and A. H. MacDonald, *Phys. Rev. B* **89**, 205414 (2014).
- [22] P. Giannozzi *et al.*, *J. Phys. Condens. Matter* **21**, 395502 (2009).
- [23] F. Wu, T. Lovorn, and A. H. MacDonald, *Phys. Rev. B* **97**, 035306 (2018).
- [24] F. Wu, T. Lovorn, and A. H. MacDonald, *Phys. Rev. Lett.* **118**, 147401 (2017).
- [25] K. Moon, H. Mori, K. Yang, S. M. Girvin, A. H. MacDonald, L. Zheng, D. Yoshioka, and S.-C. Zhang, *Phys. Rev. B* **51**, 5138 (1995).
- [26] N. Nagaosa and Y. Tokura, *Nat. Nanotechnol.* **8**, 899 (2013).
- [27] D. Xiao, M.-C. Chang, and Q. Niu, *Rev. Mod. Phys.* **82**, 1959 (2010).
- [28] C. L. Kane and E. J. Mele, *Phys. Rev. Lett.* **95**, 226801 (2005).
- [29] C. L. Kane and E. J. Mele, *Phys. Rev. Lett.* **95**, 146802 (2005).
- [30] F. D. M. Haldane, *Phys. Rev. Lett.* **61**, 2015 (1988).
- [31] C. Zhang, C.-P. Chuu, X. Ren, M.-Y. Li, L.-J. Li, C. Jin, M.-Y. Chou, and C.-K. Shih, *Sci. Adv.* **3**, e1601459 (2017).
- [32] M. Hohenadler, T. C. Lang, and F. F. Assaad, *Phys. Rev. Lett.* **106**, 100403 (2011).
- [33] X.-L. Qi, *Phys. Rev. Lett.* **107**, 126803 (2011).
- [34] J. C. W. Song, P. Samutpraphoot, and L. S. Levitov, *Proc. Natl. Acad. Sci. U.S.A.* **112**, 10879 (2015).
- [35] Q. Tong, H. Yu, Q. Zhu, Y. Wang, X. Xu, and W. Yao, *Nat. Phys.* **13**, 356 (2017).